AGU PUBLICATIONS

JGR

Journal of Geophysical Research: Solid Earth

RESEARCH ARTICLE
10.1002/2015JB012048

Key Points:
- The CMB is constantly reshaped by a dissolution-crystallization process
- Gravimetric and magnetic anomalies result from mass redistribution at the CMB
- Geopotential field anomalies suggest rates of cm/yr for changes in topography

Correspondence to:
C. Narteau,
narteau@ipgp.fr

Citation:
Mandea, M., C. Narteau, I. Panet, and J.-L. Le Mouël (2015), Gravimetric and magnetic anomalies produced by dissolution-crystallization at the core-mantle boundary, *J. Geophys. Res. Solid Earth*, *120*, doi:10.1002/2015JB012048.

Received 17 MAR 2015
Accepted 30 JUL 2015
Accepted article online 4 AUG 2015

Gravimetric and magnetic anomalies produced by dissolution-crystallization at the core-mantle boundary

Mioara Mandea[1], Clément Narteau[2], Isabelle Panet[3], and Jean-Louis Le Mouël[2]

[1]Centre National d'Etudes Spatiales, Paris, France, [2]Institut de Physique du Globe de Paris, Sorbonne Paris Cité, Université Paris Diderot, UMR 7154 CNRS, Paris, France, [3]IGN, LAREG, Université Paris Diderot, Sorbonne Paris Cité, Paris, France

Abstract Using the unique data sets provided by satellite observations, correlated temporal variations in gravity and magnetic fields over a large area extending from the Atlantic to the Indian Ocean have been recently reported. On a timescale of few years to a decade, both field variations may be linked to changes at the top of the core. Here we propose that in addition to the topography generated by the convection in the mantle, the core-mantle boundary (CMB) may be in a dynamic equilibrium state, mainly controlled by a dissolution-crystallization process of the mantle silicate rocks in the liquid alloy of the core. Due to the resulting continuous changes in CMB topography, anomalies of hundreds of nGal and tens of nT yr^{-2} might be produced by the corresponding mass redistribution and the secondary flow generated by the associated pressure field. Numerical modeling and both gravimetric and magnetic anomaly magnitudes suggest a rate of centimeters per year and a large range of length scales for the changes in the topography at the CMB.

1. Introduction

Our understanding of the Earth's deep interior is still struggling with fundamental uncertainty on the processes taking place at the core-mantle boundary (CMB). One way to get information from them is to recover flows at the top of the core that vary on a decadal timescale, using the geomagnetic secular variation. More challenging is to investigate the ability of these flows to be linked with density variations, and thus decadal gravity variations. *Dumberry* [2010] investigated the gravity changes from core flows, concluding that they are small but at the threshold of detectability in high-precision gravity measurements from space. This conclusion opens the path to new studies investigating correlated variations in gravity and magnetic fields, which would be a signature of core fluid motions.

Recently, a wealth of new high-resolution high-accuracy data have been obtained from several near-Earth satellites dedicated to describe the structure and the evolution of geopotential fields. Both gravity field intensity $g(t)$ and magnetic field $\vec{B}(t)$ show a wide range of temporal and spatial variations, and their description has required new models by means of expansions in spherical harmonics [e.g., *Bruinsma et al.*, 2010; *Lesur et al.*, 2008; *Olsen et al.*, 2010, 2014]. Based on these gravity and geomagnetic models, *Mandea et al.* [2012] found a correlation between g and $\mathrm{d}^2\vec{B}/\mathrm{d}t^2$ in some parts of the Earth's surface. Taking this correlation as granted and the removal of the effects of sources in the fluid envelopes as successful, a question is left: what can be the common source of the remaining variations of g and $\mathrm{d}^2\vec{B}/\mathrm{d}t^2$ with time constants of some 10 years, amplitudes of the order of 1 μGal for g, and some tens of nT yr^{-2} for $\mathrm{d}^2\vec{B}/\mathrm{d}t^2$?

To our knowledge, no mechanism has been proposed to explain such a correlation, at the scales considered in this study. Let us note that *Stevenson* [2012] discusses on the fluctuating gravity of the Earth's core, underlining that the nature of its dynamics is not yet well understood. Nevertheless, some investigations have been started. *Hinderer et al.* [1987] call for a kinematic pressure at the CMB, linked to the flow at the top of the core to explain the changes in the inertia momentum of the mantle. *Mandea et al.* [2012] indicate that the surface core flow – an expression of the geomagnetic secular variation – can contribute to the gravity field variations in two ways: by advection of the density heterogeneity and corresponding mass transfer or through the dynamic overpressure (associated with the flow), which deforms the overlaying elastic mantle generating a gravity anomaly (computed through a Love number formalism). But, it appeared that such a flow generated by the geodynamo mechanism and invoked to explain the deformation of the CMB is not large enough

to explain the observations. Alternatively, a geomorphic approach can be invoked. Indeed, superimposed to the large-scale dynamical topography caused by mantle convection, a dissolution-crystallization process may continuously reshape the topography of the CMB [*Narteau et al.*, 2001; *Le Mouël et al.*, 2005]. Such a physicochemical interaction between the mantle and core may lead to simultaneous gravimetric and magnetic signals through the redistribution of mass and the related flow at the top of the core. The aim of this study is to test this hypothesis, and, as an extension of this hypothesis, to quantify the rate of change in the CMB topography which could explain the observed gravimetric and magnetic signals.

The remainder of this paper is organized as follows. Section 2 describes the present-day knowledge on the gravity and magnetic field variations. The evolving topography of the CMB produced by the dissolution-crystallization process and the relevant time constants are discussed in section 3. Section 4 contains a discussion of the magnitudes of the gravimetric and magnetic signals generated by such a geomorphic process at the top of the core. The last section gives some final conclusions and directions for future work.

2. Satellite Measurements of Geopotential Fields

2.1. Satellite Observations of the Gravity Field

Since 2000, a significant improvement in measuring the gravity field from space can be highlighted, first with the CHAMP (Challenging Minisatellite Payload, 2000–2010) mission, but essentially with GRACE (Gravity Recovery and Climate Experiment from 2002) and Gravity Field and Steady-State Ocean Circulation Explorer, 2009–2013 satellite missions. Launched in 2002 and planned to last 5 years, the GRACE mission is still flying and providing the science community with measurements that reach an unprecedented precision at large to medium spatial scales. It provides the first description of the gravity field as a function of time with a global coverage, reaching a spatial resolution around 400 km [*Tapley et al.*, 2004]. Consequently, gravity models have been built and made available on a monthly or even 10 day interval basis, now up to spherical harmonic degree 80 [*Bruinsma et al.*, 2010]; short timescale variations of the gravity field have then been known for more than a decade. Aside from the tidal signals, most of these variations are attributed to the global water cycle between the oceans, the atmosphere, the cryosphere, and the continental hydrological reservoirs. Nevertheless, after these contributions are estimated and removed (at different stages in the data analysis process), solid Earth dynamics signals are left, such as those arising from large earthquakes and postglacial rebound; at larger spatial scales, decadal to subdecadal variations in Earth's gravity may find their source in the fluid core [*Mandea et al.*, 2012].

2.2. Satellite Observations of the Magnetic Field

A flourishing era for observing the Earth's magnetic field from space has started with the launch of Ørsted satellite in 1999, followed by CHAMP and SAC-C (Scientific Application Satellite-C) (2000–2013). CHAMP satellite has brought high-quality magnetic data thanks to its orbital characteristics and its highly precise payload elements. It has provided measurements over all its lifetime, allowing models of the core magnetic field ($\vec{B}$), its secular variation ($\mathrm{d}\vec{B}/\mathrm{d}t$), and secular acceleration ($\mathrm{d}^2\vec{B}/\mathrm{d}t^2$) to be computed down to length scales of some 1000 km at the Earth's surface.

Geomagnetic field models such as CHAOS (CHAMP, Ørsted and SAC-C model of Earth's magnetic field) [*Olsen et al.*, 2010, 2014] or GFZ Reference Internal Magnetic Model (GRIMM) [*Lesur et al.*, 2008, 2010] series have dramatically improved the Earth's magnetic field description. For example, the last version of CHAOS model, based on data from the satellites Ørsted, CHAMP, and SAC-C, together with magnetic observatory monthly means, describes the Earth's magnetic field up to degree 85 for the internal field at a given time, and up to degree 16 for the time-varying core field. Simultaneously, a series of GRIMM models have been derived from the CHAMP satellite data and observatory hourly means. The GRIMM-3 model of this series describes the geomagnetic field up to degree 30 for the main field, and degree 18 for the secular variation and the secular acceleration. It is important to note that changes in the trend of the secular variation of the geomagnetic field appear during the mission lifetime [*Mandea et al.*, 2010].

2.3. Flow at the Top of the Core

Assuming that there are detectable variations in both gravity and magnetic fields due to sources in the core, and more specifically at the core surface, it is appealing to question whether there are some correlations between them over the time span covered by both GRACE and CHAMP missions.

For that, we summarize the analysis by *Mandea et al.* [2012], based on the 8 years of the space missions recalled just before. One of the main difficulties is to extract from the data the (smaller) signals which would be

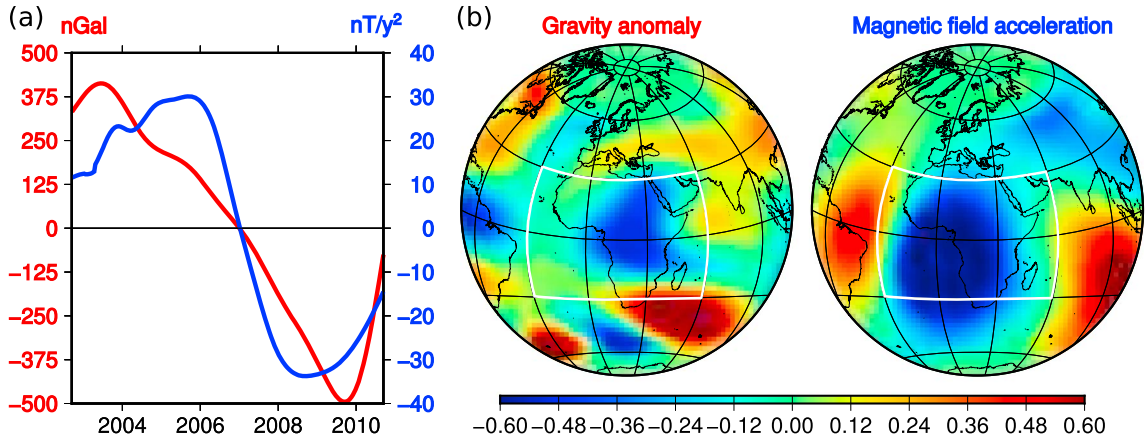

Figure 1. Common variability mode for the gravity and the magnetic time series in a portion of the Earth's surface. This mode is modeled as a space-time function $f(t) \times s(\theta, \phi)$ for each field: (a) dimensionalized time variation $f(t)$ of the gravity anomaly (red) and the secular acceleration of the vertical downward geomagnetic field component (blue); (b) nondimensionalized spatial variation $s(\theta, \phi)$ associated to the mode, for the (left) gravity anomaly and the (right) secular acceleration of the vertical downward geomagnetic field component. The white squares show the studied area. See *Mandea et al.* [2012] for more details.

attributed to the fluid core; the contributions from the lithosphere, ionosphere, and magnetosphere sources need to be filtered out from the measured magnetic field. Similarly, as said earlier, the separation of the individual components of the gravity data in the total signal is to be performed; contributions from the water cycle have first to be filtered out to detect possible mass redistribution by sources in the outer core.

After these data-filtering procedures, we can envision that changes in the gravity field might correlate with changes in the magnetic field. Performing a correlation analysis between gravity and magnetic gridded series, *Mandea et al.* [2012] show that under a region from the Atlantic to the Indian Ocean, interannual changes in the magnetic field are similar to changes in the gravity field. This conclusion has been founded on the analysis of GRACE-based and CHAMP-based data. To support the significance of the correlation, *Mandea et al.* [2012] have considered a Student's t statistical test and determined for which pair of magnetic and gravity time series the correlation is significant at the 95% confidence level. Moreover, a singular value decomposition analysis for both time series shows a comparable temporal behavior and similarities in the spatial patterns for the geomagnetic and gravity data. Figure 1 shows these temporal and spatial variations of the part of the gravity and magnetic fields interpreted as originating in the core after minimizing the contributions from surface and external sources. The figure displays large-scale magnetic and gravity fluctuation modes at the decadal timescale in a wide region beneath Africa. From the time variations of the core magnetic field, one can compute a flow at the CMB based on the well-known hypothesis of frozen flux and geostrophic flow. Then, the circulation appears to be particularly strong beneath the area framed in Figure 1b. But we will consider that the flow at the CMB is the sum of a flow which is the surface expression of the body motion generating the dynamo field, and of an independent flow that we will discuss in the following.

Independent from the dynamo flow, flows circulating in the uppermost outer core interesting a layer of thickness small compared to the core radius have already been envisioned [e.g., *Braginsky*, 1984; *Braginsky and Le Mouël*, 1993; *Jault and Le Mouël*, 1993]. More generally, various layers, more or less thick, exist or have been supposed to exist at the top of the core, from the viscous Ekman layer of theoretical thickness of the order of $\sqrt{\nu/\Omega}$ ($\approx 10^{-2}$ m for a kinematic velocity $\nu = 10^{-6}$ m^2 s^{-1} and Earth's spin $\Omega = 7 \times 10^{-5}$ rad s^{-1}) to the Braginsky's light ocean (or H layer, $H \approx 80$ km) and a seismic low-velocity zone of approximately 30–300 km thick due to compositional convection [*Garnero et al.*, 1993a; *Tanaka*, 2007; *Helffrich and Kaneshima*, 2010; *Buffett and Seagle*, 2010]. These layers are commonly associated with stratification since they are all characterized by heterogeneities in density with vertical dimensions much shorter than their horizontal length scales. But stratified layers do not prevent flow fields. *Lloyd and Gubbins* [1990] argued that if the top of the core were stably stratified, the corresponding flow would be toroidal. However, *Jault and Le Mouël* [1991] showed that this flow can be tangentially geostrophic (which requires the Lorentz forces to be negligible), with a poloidal component.

Here we consider a layer which is the seat of a flow generated by pressure change at the CMB. Independent from the dynamo main flow, this flow is driven by the dynamic evolution of a component of the CMB topography.

3. The Dynamic CMB Topography From a Dissolution-Crystallization Model

In presence of a transport mechanism, the morphology of solid-fluid interfaces is known to be strongly affected by physicochemical processes. For example, at a global scale, it is well established that weathering and bedrock-to-soil conversion have a central role in the evolution of terrestrial landscapes [*Gilbert*, 1877; *Ahnert*, 1987; *Heimsath et al.*, 1997]. In these cases, as in many others, molecular diffusion is the leading governing transport mechanism, which controls the soil production rates at the microscopic length scale. Inspired by these small-scale surface processes and their impact on landscape dynamics, *Narteau et al.* [2001] developed a numerical model of a dissolution-crystallization mechanism acting on the morphology of the CMB, a major terrestrial interface between the dense liquid alloy of the outer core and the solid crystalline silicate of the mantle.

3.1. Infiltration, Dissolution, and Crystallization at the Base of the Mantle

The model discussed below relies on the idea that the liquid iron of the outer core can corrode the overlying mantle material as the hot unsaturated liquid alloy migrates upward by capillarity and preferentially penetrates and dissolves grain boundaries of the silicate rocks [*Poirier and Le Mouël*, 1992]. According to this mechanism, the order of magnitude of the height reached by the fluid is given by the surface tension difference ($\approx 0.8\ \mathrm{J\ m^{-2}}$) divided by the fluid density ($\approx 10^4\ \mathrm{kg\ m^{-3}}$) times gravitational acceleration ($\approx 10\ \mathrm{m\ s^{-2}}$) and channel width. Following *Otsuka and Karato* [2012], the channels containing the liquid are of the order of a few microns thick, or thinner. Then, a typical height estimate of few meters may be retained.

Concerning the dissolution mechanism itself, *Poirier and Le Mouël* [1992] do suppose that individual grains can disintegrate. Indeed, there is observational evidence of infiltration of liquid core in grain boundaries of silicate and oxide minerals [e.g., *Poirier et al.*, 1998] and of enrichment of iron in the dissolved oxygen, which means destruction of the oxygen framework of the crystals. When this oxygen framework is destroyed, the whole structure falls apart and it can be said that the mineral is dissolved. We can use an analogy, however partial, with the weathering of granite: water infiltrates between the grains and progressively disintegrates the rock. Coming back to the CMB, *Poirier and Le Mouël* [1992] then considered that individual grains could be dissolved into iron liquid, which implicitly assumed that all the rock-forming elements are evenly dissolved. Recent high-pressure experiments, however, demonstrated preferential dissolution for silicon, oxygen, and iron and very limited dissolution for magnesium, from the mantle minerals (i.e., magnesium-rich silicate perovskite and ferropericlase) into the core liquids [*Takafuji et al.*, 2005; *Ozawa et al.*, 2009]. This indicates that any individual mineral is not dissolved into the core, but some elements such as Si and O are preferentially extracted from the minerals, i.e., partitioning of the elements between the mantle and core [*Ozawa et al.*, 2009]. This process may eventually corrode the lower mantle surface because the extraction of those elements may destroy the mineral structure. As such, the dissolution of the elements from the lower mantle and subsequent crystallization would modify the geometry of the core-mantle interface. Note that which mineral is dissolved is not so important; they are all silicates and oxides, with a framework of oxygen atoms.

A second point needs consideration: the role of compaction. Sintering is controlled by self-diffusion in solid minerals. It is a slow process, much slower than infiltration. Following *Poirier and Le Mouël* [1992], the time t_h required for the liquid to reach a height h was estimated as $6.9 \times 10^{-3}\ h^2/D$, where D is the coefficient of diffusion of oxygen in liquid iron. For $h = 1$ m and $D = 3 \times 10^{-9}\ \mathrm{m^2\ s^{-1}}$, it gives a timescale of approximately 26 days. It is not adventurous to think that the time constants of compaction are much larger so that it does not impede infiltration and dissolution of the mantle minerals.

Other researchers have dealt with the infiltration of liquid core into the mantle [e.g., *Kanda and Stevenson*, 2006; *Otsuka and Karato*, 2012]. The objective of *Kanda and Stevenson* [2006] was to explore the possibility of maintaining a conducting layer at the base of the mantle, which could couple the outer core and the mantle through Lorentz torques. They propose a suction mechanism that maintains a porous medium with a thickness of 1 km above the CMB in which the interconnected pore space is partly or entirely filled with liquid iron; infiltration of liquid core occurs by percolation. The so-obtained mantle side-conducting layer would be stable for periods similar to mantle convection times or longer. This mechanism allows much more liquid iron infiltration into the lower mantle compared to capillarity action. Nevertheless, in regard to the objectives aimed

Table 1. Physical and Model Parameters Used in the Cellular Automaton Model of the CMB[a]

		Units	Value
	Physical Parameters		
d	Grain size	m	10^{-2}
D	Diffusion coefficient	$m^2\ s^{-1}$	3×10^{-9}
ρ_m	Mantle density	$kg\ m^{-3}$	5.6×10^3
ρ_c	Outer core density	$kg\ m^{-3}$	10^4
ρ_s	Saturated fluid density	$kg\ m^{-3}$	8.4×10^3
	Model Parameters		
H	System height	l_0	800
L	System length	l_0	2×10^4
Λ_C	Transition rate for crystallization	$1/t_0$	1
Λ_L	Transition rate for dissolution	$1/t_0$	1
Λ_T	Transition rate for transport	$1/t_0$	3
a	Vertical transport anisotropy	∅	5×10^{-2}
n	Saturation ratio	∅	3
	Model Units		
l_0	Elementary length scale	m	l_0
t_0	Elementary timescale	s	$\tilde{\Lambda}_T l_0^2/D$

[a] $\{l_0, t_0\}$ are the length scale and timescale of the model. Transition rates for dissolution, crystallization, and diffusion are chosen close to one with $\Lambda_L = \Lambda_C < \Lambda_T$. All expressed in units of $1/t_0$; only their relative values are of significance. a is a constant to take into account gravity in the transport mechanism (see Figure 2). We also take $n = (\rho_c - \rho_m)/((\rho_c - \rho_s)$.

at by the authors, the layer obtained by using the suction model does not cover the entire CMB and may be too thin to yield high enough conductance.

Otsuka and Karato [2012] consider the deep infiltration of molten iron into the mantle to explain the low seismic wave velocities and high electrical conductivity at the base of the mantle. Contacts of (Mg, Fe)O minerals with liquid iron could generate morphological instabilities and cause the formation of blobs of iron-rich liquid. Transcrystalline melt migration is then an efficient mechanism of chemical transport, which could explain fluid migration over tens of kilometers away from the CMB. Incidentally, *Otsuka and Karato* [2012] estimate that the extent of iron penetration by the suction mechanism of *Kanda and Stevenson* [2006] would be less than a meter, too small to cause any appreciable effect. Comparing the outputs of the above mechanisms with the one of an infiltration-dissolution-crystallization model, it might be argued that we invoke a small effect and ignore larger ones. But it fits the mechanism of building a metric relief at the CMB that we consider in the present paper (see comment at the end of the conclusion).

3.2. A Discrete Model for Dissolution-Crystallization of the CMB

The model used is a cellular automaton generated by Real-Space Cellular Automaton Laboratory (ReSCAL), a free software under GNU general public license [*Rozier and Narteau*, 2014]. Cellular automata are systems that iteratively evolve on a grid according to local interaction rules. Here our model consists of a regular square lattice of cells encoding the local state of the physical environment under consideration. At the elementary length scale of the lattice, each cell has a characteristic length l_0 (Table 1). As shown in Figure 2, we consider three states: the solid state corresponds to the silicate material of the mantle and the two liquid states represent, respectively, the saturated and unsaturated iron alloy in the outer core. Dissolution, crystallization, and diffusive transport are then simulated using three independent sets of doublet transitions and three transition rates $\{\Lambda_L, \Lambda_C, \Lambda_T\}$. These transition rates translate into the model the characteristic timescales of the underlying physical/chemical processes. They are all expressed in units of $1/t_0$, where t_0 is the characteristic timescale of the model (see below). The iteration scheme behaves like a dynamical system: its evolution is entirely defined as a stationary process based only on the knowledge of the present cellular space and the transition rate values [*Narteau et al.*, 2001; *Narteau*, 2007]. Practically, this scheme can be regarded as a generalized Poisson process or a specific type of continuous-time Markov process.

The model parameter values are set according to three physical constraints. First, the typical grain size d of the silicate minerals give the elementary length scale l_0 of the square lattice. Second, the molecular diffusion

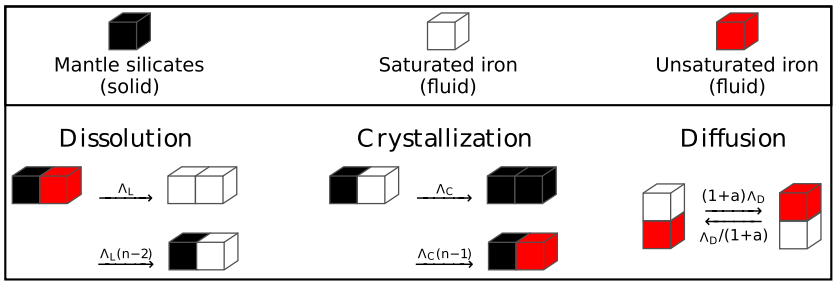

Figure 2. A cellular automaton model of the dynamic topography of the CMB. At the elementary scale l_0 of the model, three states are used to represent the solid silicate of the mantle (black cells), the saturated liquid iron alloy of the outer core (white cells), and the unsaturated liquid iron alloy of the outer core (red cell). One cell of mantle saturates n cells of core fluid in light elements. Transitions for dissolution, crystallization, and diffusion (transport) are represented by a set of doublet transitions. These transitions ensure conservation of mass. $a > 0$ is a constant that introduces the effect of gravity into the transport mechanism. The horizontal transition rate for diffusion is equal to Λ_T. Here we only show the transitions along a given direction in 2-D. In 3-D, there are six times more transitions (i.e., three orientations of doublets and for each of them two symmetric doublets when the states of the cells are interchanged). All transition rates $\{\Lambda_L, \Lambda_C, \Lambda_T\}$ are expressed in units of $1/t_0$, where t_0 is the characteristic timescale of the model (see Table 1).

coefficient D of the light element in the unsaturated liquid alloy determines the characteristic timescale of the model using the relation

$$t_0 = \frac{\tilde{\Lambda}_T l_0^2}{D}, \tag{1}$$

where $\tilde{\Lambda}_T$ is the dimensionless Λ_T value (i.e., $D = \tilde{\Lambda}_T\ l_0^2\ t_0^{-1}$). Third, the density ratios between the different states under consideration give the number n of unsaturated liquid cells that reach saturation when a silicate cell of the mantle is dissolved. The usual parametrization of the model and the physical parameter values are presented in more details in Table 1. All the numerical results reported below are expressed in units of $\{l_0, t_0\}$ using $d = l_0 = 1$ cm, $D = 3 \times 10^{-9}$ m^2 s^{-1}, and $\Lambda_T t_0 = 3$. We have then $t_0 = 10^5$ s $= 3.2 \times 10^{-3}$ years.

Figure 3a shows a realization of a 2-D model starting from a flat interface between the solid silicate rocks and the liquid iron alloy. This example indicates that coupled with a diffusive transport mechanism, dissolution and crystallization processes operating at a microscopic scale may generate a topography with a wide range of wavelengths (see below for a discussion of Figure 3).

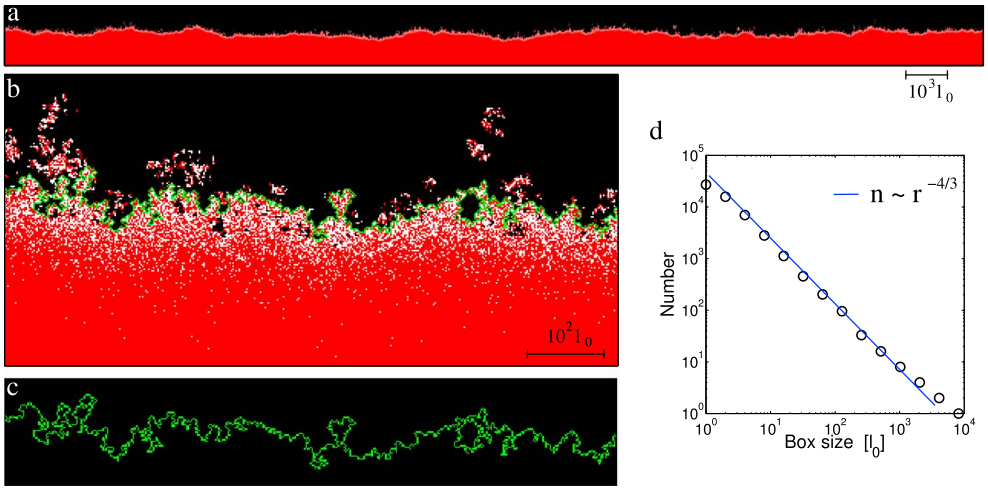

Figure 3. Characterization and localization of the CMB in the cellular automaton model. (a) Vertical section of a cellular automaton model with a length L of 2×10^4 cells and a height of 800 cells. Red, white, and black cells are for nonsaturated liquid iron, saturated liquid iron, and solid silicate, respectively. Note the irregular undulations of the interface between the solid silicate of the mantle and the liquid iron of the core. (b) A zoom on a vertical section of 400×250 cells. Solid cells of the solid-liquid interface are shown in green. (c) The solid cells composing the solid-liquid interface (i.e., all cells which are part of the giant cluster of solid cells and in contact with the giant cluster of liquid iron cells). (d) The fractal dimension of the solid-liquid interface using a box-counting method [*Pfeifer and Obert*, 1989].

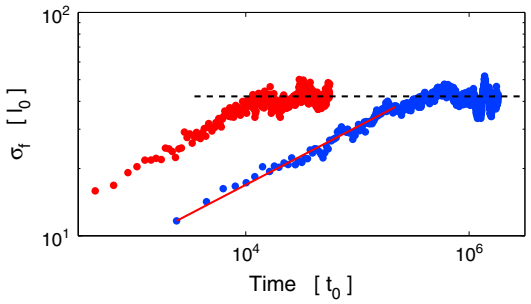

Figure 4. Evolution of the amplitude of the CMB relief in the cellular automaton model. Starting from a flat interface with a length L of 2×10^4 cells, the thickness of the CMB relief increases until it reaches a steady state amplitude: $\Lambda_T t_0 = 3$ (blue); $\Lambda_T t_0 = 30$ (red) (see Table 1 for other parameter values). The solid red line is a power law with a slope of 1/5. The black dashed line indicates the steady state amplitude of 42 l_0 that scales with the horizontal length of the cellular space (Figure 5). Higher diffusion rates reduce the characteristic timescale of the dynamic topography.

3.3. The CMB as a Gradient Percolation Frontier

In this section, we analyze the morphology of the solid-liquid interface to show that the cellular automaton model presented above belongs to the universality class of gradient percolation [*Sapoval et al.*, 1985]. Based on the concept of diffusion front [*Gouyet and Rosso*, 2005], the gradient percolation theory provides a complete framework to explain the spontaneous emergence of a random interface with a fractal geometry. This theory can be used to describe a large set of dynamical systems related to diffusion or corrosion processes (see references 25–41 in *Gouyet and Rosso* [2005]). This is particularly true in 2-D because the outputs of dynamical systems may be directly compared to exact analytical solutions.

To describe the most important features of the gradient percolation theory in 2-D, let us consider a rectangular regular lattice of cells for which the percolation parameter, i.e., the probability for a site to be occupied, increases linearly from 0 to 1 from the bottom ($\xi = -N$) to the top ($\xi = N$). Thus, all cells of the upper boundary are occupied, while those of the lower boundary are vacant. Overall, the gradient naturally creates two giant clusters of connected occupied cells at the top and connected vacant cells at the bottom. Each cluster may include smaller clusters of the other type of cells in such a way that a given cell is either connected to its giant cluster or part of an island within the giant cluster of the other type. Most important for our present purpose, the two clusters are in contact with one another and there is a unique interface between them [*Essam*, 1972]. This unique interface can be seen in Figures 3b and 3c. Usually called the percolation front, it exhibits scaling properties related to the critical exponents of the percolation theory [*Stauffer and Aharony*, 1994]. For example, it has a fractal dimension $\nu_f = 4/3$ [*Grossman and Aharony*, 1987] and its average thickness is

$$\varsigma = N^{\frac{\nu_f}{1+\nu_f}} = N^{\frac{4}{7}}. \tag{2}$$

Thus, the front stays in average at the same depth, but it may have vertical fluctuations of the order of ς.

In our case, the solid-liquid interface (i.e., the CMB) is defined as the percolation front between the giant cluster of silicate cells at the top and the giant cluster of liquid iron cells at the bottom (Figures 3b and 3c). Thus, we can identify and precisely locate the compositional boundary where abrupt changes in density occur. In general, the two giant clusters of solid and liquid cells are obtained using nearest neighbor connectivity at the elementary length scale of the cellular automaton model. For the specific example shown in Figure 3c, the solid-liquid interface has a fractal dimension of 1.31 ± 0.05. In all cases, this fractal dimension is very close to 4/3, indicating that our specific dynamical system can be indeed replaced in the general context of the percolation theory [*Sapoval et al.*, 2004].

Using the outputs of the model, we systematically quantify the average depth $\bar{z}_f$ and width (or thickness) σ_f of the synthetic CMB using all the cells that form the percolation front. Basically, these two parameters are the first and second moments of $n_f(z)$, the depth distribution of the cells that compose the solid-liquid interface:

$$\bar{z}_f = \frac{\sum_{z=1}^{H} z n_f(z)}{\sum_{z=1}^{H} n_f(z)}, \quad \text{and} \quad \sigma_f^2 = \frac{\sum_{z=1}^{H} (z - \bar{z}_f)^2 n_f(z)}{\sum_{z=1}^{H} n_f(z)}, \tag{3}$$

where H is the height of our cellular space (see Table 1). Starting at $t = 0$ with a flat interface between mantle and iron cells, Figures 3a and 3b show the cellular space at $t/t_0 = 1.8 \times 10^6$. For the duration of this simulation, Figure 4 shows the evolution of the thickness of the solid-liquid interface as measured by equation (3). There are clearly two stages. Over short times, the first stage is characterized by a power law increase of the

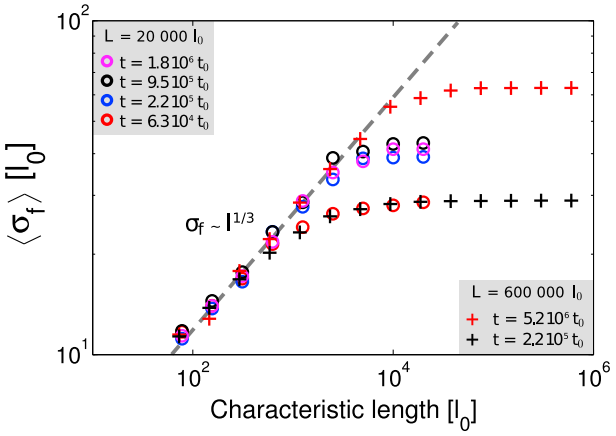

Figure 5. Vertical amplitude of the CMB with respect to the horizontal length of the cellular automaton model. The initial condition at $t = 0$ is a flat interface. At each time, we divide the cellular space into smaller subsections using nonoverlapping sliding windows of length $l_i = L/2^i$. For each length scale $i \in [0, 1, 2, \ldots]$ and within each section, we calculate the thickness of the CMB (equation (3)). We report on the graph the mean value $\langle \sigma_f \rangle$ averaged over the 2^i sections. Crosses and circles show that the system dynamics does not depend on its horizontal length. However, this length controls the vertical extent of the topography of this interface. The values for $t/t_0 \geq 2.2 \times 10^5$ indicate that the CMB has reached a steady state amplitude ($42\, l_0$ as measured in Figure 4). The dashed line is $\langle \sigma_f \rangle = 2.5\, l^{1/3}$.

width of the interface ($\sigma_f \sim t^{1/5}$). Over longer times, the width of the interface remains statistically constant around an average value of $42\, l_0$, despite important fluctuations. The system has reached a steady state with a characteristic value of the width of the solid-liquid interface, i.e., $42\, l_0$.

In geophysics, predictive scaling relationships are often used to make the results applicable to Earth's conditions [e.g., *Christensen and Aubert*, 2006]. Here to extrapolate the morphological properties of the modeled interface to the size of the CMB, it is necessary to analyze how the width of this compositional boundary depends on the length L of the system. With this goal in mind, we successively analyze different sections of the solid-liquid interface using nonoverlapping horizontal sliding windows in a range of length $l_i = L/2^i$, $i \in [1, 2, 3, \ldots]$. For a given length scale l_i, we estimate the width σ_f of the solid-liquid interface of all the 2^i

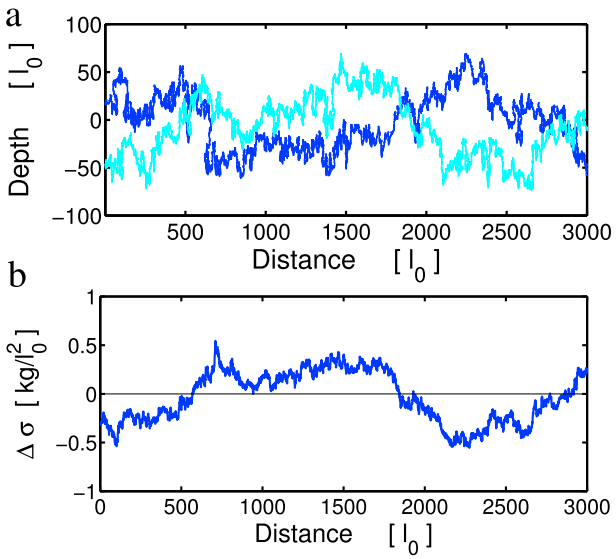

Figure 6. The dynamic topography of a steady state CMB in the cellular automaton model: (a) the solid cells composing the solid-liquid interface at two different times separated by $3.5 \times 10^6\, t_0$. The mean depth is arbitrarily set to 0. (b) Changes in density of individual column between the two configurations of the CMB shown in Figure 6a; the mass of a vertical column of section l_0^2 at a given time is the sum of the mass of all cells that compose this column. Thus, changes in topography are translated into changes in the surfacic distribution of mass.

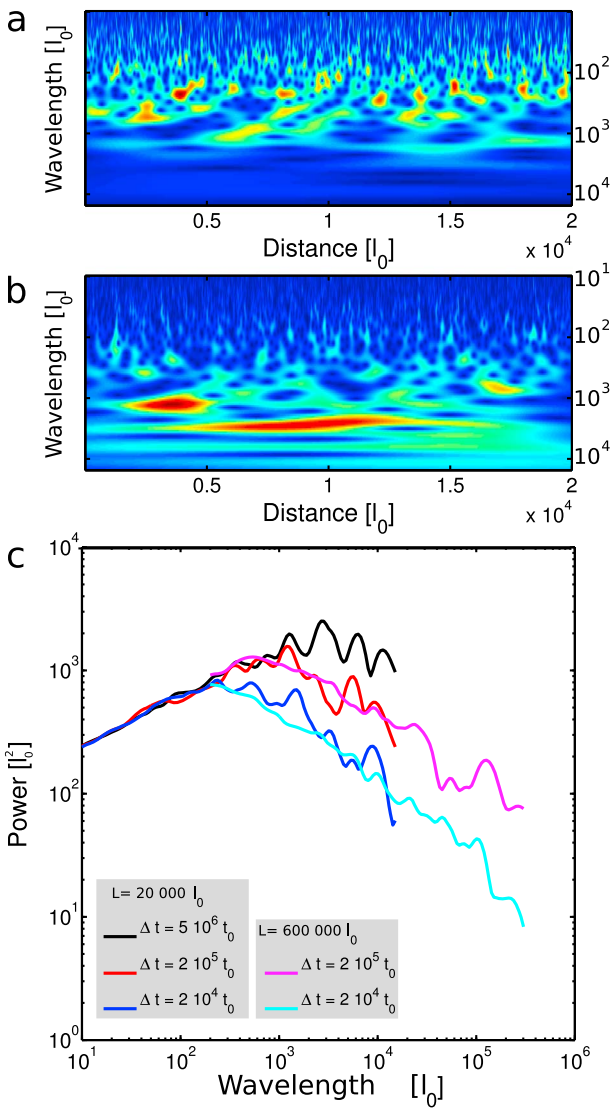

Figure 7. Spectral analysis of the changes in the horizontal mass density profiles. Wavelet power spectrum of mass redistribution for two time intervals of (a) 2×10^4 t_0 and (b) 5×10^6 t_0. (c) Evolution of the global wavelet spectrum of the mass redistribution. It takes a longer time to reshape the CMB on increasingly larger wavelengths. However, as shown by the power law decay over long wavelengths, all length scales are rapidly activated by the dissolution-crystallization process.

sections. Averaging over all sections, Figure 5 shows how the mean value of this width $\langle \sigma_f \rangle$ is evolving with respect to the characteristic length scale l_i. For larger length scales, there is a plateau whose ordinate is directly related to the length L of the cellular space. It shows that the horizontal length of the system commands the vertical amplitude of the CMB relief (Figure 4). However, for smaller length scales, there is a systematic increase of the mean width of the interface with respect to the horizontal length l_i of the different sections. More exactly, we find that the amplitude of the topography increases as a power law with an exponent 1/3. Such a scaling law can then be used to extrapolate the vertical amplitude of the CMB topography to the characteristic length scale of the outer core. For example, using a grain size d of 1 cm, it predicts a maximum amplitude of 12 m (25 m) over a distance of about 10^3 km (10^4 km).

3.4. Time Constants of the Dynamic Topography

Using the results of the above numerical simulations, we now focus on the characteristic timescales of the changes in the topography produced at the CMB by the continuous action of the dissolution-crystallization process. Hence, we concentrate on the dynamics of the solid-fluid interface when it has reached its steady

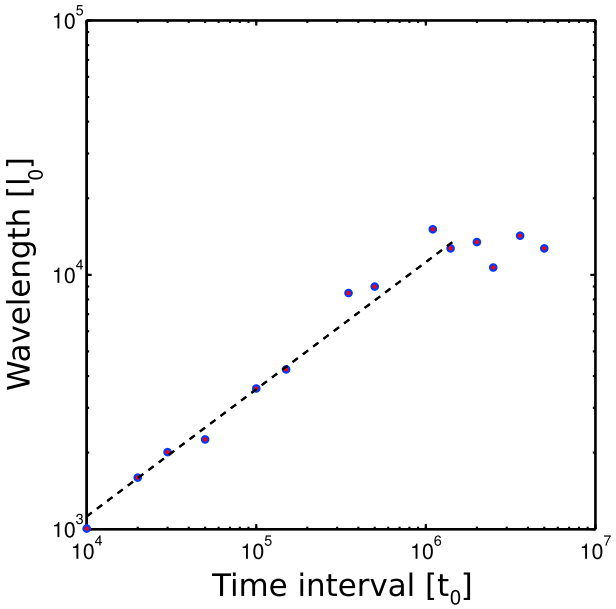

Figure 8. The relation between timescale and length scale for a complete change in the horizontal mass density profile. For a given time interval Δt, we report the most energetic wavelength λ in the global wavelet spectrum (Figure 7c). The dashed line is $\lambda = 5.3\,\Delta t^{1/2}$. The saturation is a finite size effect observed when the entire solid-fluid interface of the cellular automaton model has been reshaped.

state characterized by systematic temporal fluctuations of mean depth and width of 42 l_0 (Figures 4 and 5). For example, Figure 6a shows the CMB generated by the cellular automaton model at two different times separated by 3.5×10^6 t_0. During this time interval, a complete reorganization of the solid-fluid interface is responsible for significant variations of the horizontal mass density profile (Figure 6b). Obviously, this redistribution of mass needs time, since it requires not only both dissolution and crystallization but also a transport mechanism to move the dissolved material across the system.

Figures 7a and 7b show the wavelet analysis [*Holschneider*, 1995] of the redistribution of mass for two different time intervals. For a short time interval, changes in the horizontal density profile are restricted to short wavelengths, whereas there is little difference for long wavelengths. But for a long time interval, long wavelengths are excited and the changes in density affect the entire system. To quantify the relationship between time and length scales of the redistribution of mass, we use the global wavelet spectrum of the changes in density (see Figure 7c) and select the most energetic wavelength corresponding to different time durations. We find that the required time to reshape the solid-liquid interface scales as the square of the wavelength (Figure 8). Not surprisingly, this is characteristic of a diffusion process, which can be directly related to the transport mechanism implemented at the elementary scale of the model.

Now considering that diffusion of light elements in the liquid iron alloy of the core controls changes in topography, we can use the scaling of the heat equation to relate the timescale and length scale relevant to the dynamics of the mass density profile. Considering again the molecular diffusion coefficient D, it states that a perturbation can be felt at a distance l after a time delay

$$\Delta t \sim l^2/D. \tag{4}$$

Using this expression or the numerical scaling law shown in Figure 8, we find that topographic changes at length scale of 10^3 km (i.e., 10^8 l_0 using $d = 10^{-2}$ m) may require billions of years. This is obviously much too high to be relevant for the time constants involved in our observations (see section 2). But, this timescale is directly proportional to the characteristic timescale t_0 of the model, and therefore, sensitive to the scale setting parameters (equation (1)). Then, keeping constant the relative values of the transition rate $\{\Lambda_C, \Lambda_L, \Lambda_T\}$, the diffusion coefficient D may be increased by orders of magnitude to reduce by the same factor the timescale of the changes in the mass density profile at the CMB. Unfortunately, for the Earth's interior, there is no means to significantly enlarge the D value [*Poirier*, 2000].

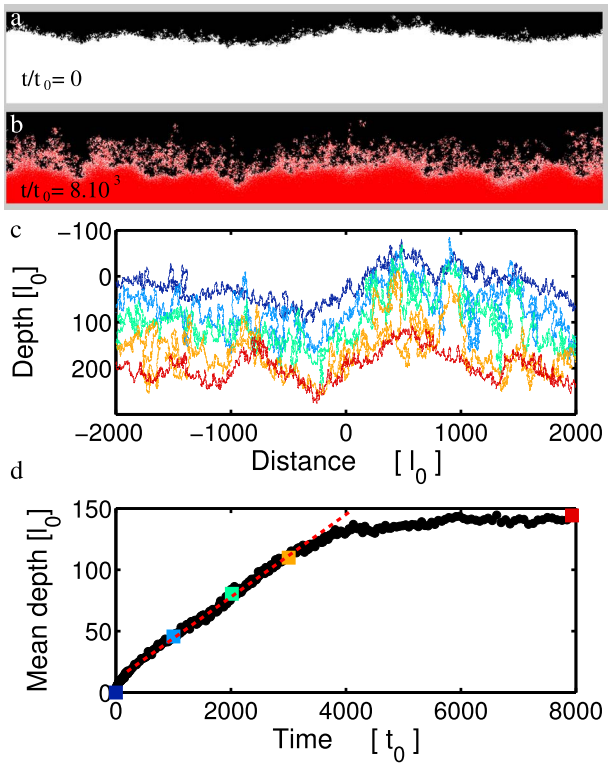

Figure 9. The evolution of the depth of the CMB in depositional settings. (a) The initial condition at $t = 0$ is generated from a steady state configuration of the CMB by changing all the fluid cells into their saturated state. (b) Same portion of the CMB as in Figure 9a at $t/t_0 = 8000$ when the dynamic topography has reached its new steady state at a deeper depth. (c) The CMB at different times (see symbols in Figure 9d). Cells that form the percolation front at each time are shown with the same color. (d) Evolution of the depth of the CMB from the initial condition (Figure 9a) to its steady state (Figure 9b). In the presence of a high concentration of saturated cells, the crystallization process dominates and the interface progressively reaches deeper into the liquid phase. A constant deposition rate of 0.03 l_0/t_0 is observed before the system reaches again a steady state (dashed red line). Colored squares in Figure 9d correspond to the interface shown in Figure 9c.

Another way of getting faster changes in the topography is to modify the parametrization of the proposed model. The main control parameter is then the ratio between the intensity of the dissolution-crystallization process and the intensity of the transport mechanism. For example, we can increase the Λ_T value, keeping constant the $\{\Lambda_C, \Lambda_L\}$ values to enhance the transport mechanism with respect to the molecular diffusion, which still determines the characteristic timescale of the dissolution-crystallization process itself. In this case, Figure 4 shows that topographic changes indeed occur faster. Hence, a model in which the transport mechanism is based on a turbulent diffusion coefficient entering Λ_T may significantly reduce the characteristic timescales for the evolution of the mass density profile. In fact, in response to a shear flow, the turbulent diffusion coefficient may be many orders of magnitude greater than the molecular diffusion coefficient, in particular, in the case of a rough boundary layers [e.g., *Hinze*, 1972; *Ligrani and Moffat*, 1986]. Unfortunately, such large values cannot be tested in the model because of the current computational limits.

The distribution of the light elements at the top of the outer core may also affect the evolution the CMB [*Buffett et al.*, 2000]. For example, specific flow conditions can locally concentrate the dissolved silicate material, leading to the development of a large depositional basin. To analyze such conditions, we run a simulation starting from an initial condition in which all the fluid cells of a steady state configuration of the CMB are saturated (Figure 9a). Thus, the crystallization process dominates and the deposition promotes the growth of the CMB to greater depths (Figure 9c). Finally, the CMB reaches a new steady state with constant depth and thickness. Before, there is a transient period during which the deposition rate is constant with a value of 0.03 l_0/t_0. Using the usual parametrization of the model ($d = 10^{-2}$ m, $D = 3\times10^{-9}$ m^2 s^{-1}), it corresponds to a

deposition rate of 10 cm yr^{-1}. Thus, the model used in a specific depositional setting predicts high deposition rates that may lead to rapid variations of the mass density profile due to rapid changes in topography of the CMB (i.e., 30 cm in 3 years).

4. Gravimetric and Magnetic Anomalies Generated by Dissolution-Crystallization at the CMB

As a result of the dissolution-crystallization process, the CMB may exhibit a fractal topography that constantly evolves. Such a dynamic topography may generate gravimetric and magnetic signals at the surface of the Earth.

4.1. The Magnitude of the Gravimetric Signal Generated by the CMB Topography

Figure 2 shows that at the boundary between the modeled core and mantle, a layer with a thickness of a few tens of centimeters contains both core liquid, with a density $\rho_c = 10^4$ kg m^{-3}, and silicates, with a density $\rho_m = 5 \times 10^3$ kg m^{-3}. The topography as pointed out earlier, although small in vertical amplitude, is efficient in generating a gravity anomaly due to the large contrast of density between the iron of the core and the silicates of the mantle, i.e., $\Delta\rho = \rho_c - \rho_m \approx 5 \times 10^3$ kg m^{-3}.

To compute the order of magnitude of this gravity anomaly at the Earth's surface, which strongly depends on the length scale of the topography, let us consider the spherical harmonics expansion of the fractal CMB topography:

$$h(\theta,\phi) = \sum_{n,m} h_{nm} Y_{nm}(\theta,\phi), \tag{5}$$

where h_{nm} is in meters and $Y_{nm}(\theta,\phi)$ are the fully normalized surface spherical harmonics of degree n and order m. At the GRACE resolution, the surfacic mass anomaly (i.e., mass per unit area) carried by this topography with respect to the reference CMB is $\Delta\sigma(\theta,\phi) = \Delta\rho \times h(\theta,\phi)$ (the thin layer approximation holds). The gravity potential resulting from the direct Newtonian attraction of this load, referred to the CMB, is

$$V(r,\theta,\phi) = \sum_{n,m} \left(\frac{r_b}{r}\right)^{n+1} V_{nm} Y_{nm}(\theta,\phi), \tag{6}$$

where r_b is the CMB radius. In addition, we have

$$V_{nm} = \frac{4\pi G r_b}{2n+1} \times \Delta\rho \times h_{nm}, \tag{7}$$

with $G = 6.67 \times 10^{-11}$ m^3 kg^{-1} s^{-2}. The amplitude of the corresponding gravity anomaly δg at the Earth's surface is derived using $\delta g\big]_{r=r_a} = -\frac{\partial V}{\partial r}\Big]_{r=r_a}$, where r_a is the Earth's surface radius. Thus, the harmonic component of degree n and order m of the gravity anomaly at the Earth's surface is

$$\delta g_{nm}(r_a,\theta,\phi) = (n+1)\left(\frac{r_b}{r_a}\right)^{n+2} \frac{4\pi G}{2n+1} \times \Delta\rho \times h_{nm} Y_{nm}(\theta,\phi). \tag{8}$$

For increasing degrees, this relation is approximately equal to

$$\delta g_{nm}(r_a,\theta,\phi) \approx 2\pi G \times \Delta\rho \times h_{nm} \left(\frac{r_b}{r_a}\right)^{n+2} Y_{nm}(\theta,\phi). \tag{9}$$

The geoid anomalies N at the Earth's surface are derived as $N = \frac{V}{g_0}\Big]_{r=r_a}$, where g_0 is the average gravity attraction at the Earth's surface: $g_0 = \frac{4}{3}\pi G r_a \bar{\rho} \approx 9.8$ m s^{-2} and $\bar{\rho} = 5517$ kg m^{-3} is the average density of the Earth.

Taking $n = 6$, which corresponds to a resolution at the Earth's surface close to 3300 km, $h_n(\theta,\phi) = \sum_m h_{nm} Y_{nm}(\theta,\phi)$ and $\|h_n\| = 1$ m, the obtained amplitudes reach

$$\delta g_6(r_a,\theta,\phi) = 1.57 \times 10^{-8} \text{ m s}^{-2} = 1570 \text{ nGal},$$

and

$$\delta N_6(r_a,\theta,\phi) = 1.57 \text{ mm}.$$

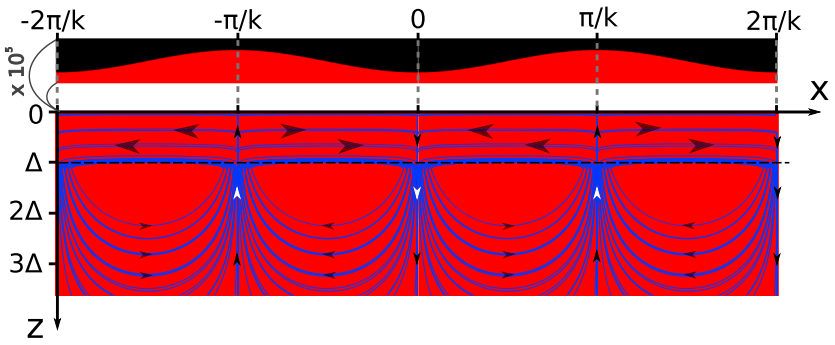

Figure 10. Streamlines of the 2-D flow model at the top of the CMB (see equations (15)–(18) and *Braginsky and Le Mouël* [1993]). The arrow size indicates roughly the relative flow strength. A strong shear of the component v_x takes place at $z = \Delta$. A zoom of the periodic CMB topography responsible for this flow is shown at the top of the figure. A vertical dilatation of 10^5 is applied: $\Delta = 30$ km and a the relief amplitude $h = 30$ cm.

The computed amplitudes are of the order of those discussed in section 2, for approximately 30 cm of topography at the degree 6 resolution, which is about 1800 km at the CMB.

The variation in the gravity potential due to the direct attraction of the mass anomaly carried by the CMB topography creates a volumic force in the whole Earth. At the considered timescales, it induces elastic deformations in order to reach a new state of equilibrium. In addition, it creates a surfacic force at the CMB (a pressure), to which both the mantle and the core react via further deformations. Classically, the deformations due to gravity potential or surface pressure changes, and the corresponding secondary gravity variations, are modeled by solving the elastogravitational equations [*Alterman et al.*, 1959]. They comprise the momentum equation, the mass conservation equation, and the Poisson equation, typically assuming an elastic compressible mantle and an inviscid fluid core. The obtained system of equations is, however, not valid in the fluid core, which is supposed to remain in hydrostatic equilibrium in the deformed state (see, for instance, *Chinnery* [1975] among the many references addressing this difficulty). This approach has been applied in order to compute the gravity signal of the elastic mantle deformations caused by a fluid overpressure at the core-mantle boundary arising from tangentially geostrophic core motions [*Dumberry and Bloxham*, 2004; *Greff-Lefftz et al.*, 2004]. More recently, it has also allowed to estimate the gravity variations from decadal changes in lateral density heterogeneities within the fluid core [*Dumberry*, 2010]. The gravity effect of the mantle deformations caused by the gravity potential change appeared to be small as compared to the direct attraction of the forcing mass anomaly [see *Dumberry*, 2010, Figure 3].

In our case, the forcing arises from a topographic mass anomaly at the boundary between the mantle and the core. As the deformations caused by the associated gravity potential variations should only have a small impact on the total gravity signal [*Dumberry*, 2010], the question is how the pressure variations at the CMB due to this mass anomaly are accommodated by the mantle and the core. Solving the elastogravitational equations as previously described and assuming hydrostatic equilibrium in the fluid core, the mantle responds instantaneously to the pressure variation at its base; it nearly compensates the direct attraction of the CMB topography, and the total gravity signal is reduced by a few orders of magnitude (M. Greff-Lefftz and L. Métivier, personal communication, 2014). However, the CMB mass anomaly can induce dynamic motions within the core, not accounted for by the elastogravitational system. Topographic highs at the CMB (i.e., mass and pressure excess) could be dynamically supported by core fluid upwellings, while topographic lows (i.e., mass and pressure default) could be underlain by downwellings (Figure 10). The total overpressure at the base of the mantle would then be negligible, canceling the mantle response. In this extreme case, the direct Newtonian attraction of the CMB rugosity would finally provide an order of magnitude of the total gravity signal at the Earth's surface. Let us, however, underline that this line of reasoning is, at this stage, only tentative; a quantitative modeling of the Earth's mass redistribution and pressure variations, on the mantle side and on the dynamic core side, in response to such a forcing at the CMB, remains to be addressed.

4.2. The Related Flow and Magnetic Signal Induced by a Dynamical Topography at the CMB

Let us consider the topography of the CMB $h(\theta, \phi)$ — or rather a smoothed version of this topography since the geometric attenuation considerably reduces the effect of the short-scale components at the Earth's surface.

In response to changes in elevation, a pressure field $\Pi(\theta, \phi)$ is imposed upon the core surface. Considering a harmonic component of order n (see section 3.4), we have

$$\Pi_n(\theta, \phi) = g\Delta\rho \times h_n(\theta, \phi). \tag{10}$$

Relying on the length scale of our observations and the amplitude of the gravimetric anomaly (Figure 1), we take $n = 6$ and $\|h_6\| = 0.3$ m ($\|h_6\| = 3$ m) to compute $\Pi_6 = 1.5 \times 10^4$ Pa ($\Pi_6 = 1.5 \times 10^5$ Pa).

4.2.1. Estimation of the Associated Flow Velocity at the Top of the Core

To sustain the topographic anomalies of the CMB over a timescale of decades, a flow must be present in the upper layers of the core (see section 4.1). An order of magnitude of the (horizontal) velocity of this flow $\vec{v}$ at the top of the core can be obtained by writing that the corresponding dynamic pressure p balances the pressure Π of the bumps in topography (see equation (10)):

$$p(\theta, \phi) = -\Pi(\theta, \phi). \tag{11}$$

Supposing a tangentially geostrophic approximation [e.g., *Le Mouël*, 1984], the (horizontal) velocity $\vec{v}$ is linked to the pressure field at the core surface by

$$\rho_c \vec{v} = \frac{1}{2\Omega \cos(\theta)} \vec{n} \wedge \vec{\nabla} p, \tag{12}$$

where $\vec{\Omega}$ is the Earth spin. Let us look for an order of magnitude of this flow velocity considering again a spherical harmonic of degree n, we have

$$v \approx \frac{1}{2\rho_c \Omega} \times \frac{n\,\Pi_n}{2\pi r_b}. \tag{13}$$

For $n = 6$, $\Omega = 7 \times 10^{-5}$ s^{-1}, $\|h_n\| = 0.3$ m ($\|h_n\| = 3$ m), and the corresponding Π_6 value computed above, we get $v \approx 2.9 \times 10^{-3}$ m s^{-1} ($v \approx 2.9 \times 10^{-2}$ m s^{-1}).

For a given Π value, equation (13) gives the flow velocity at the CMB, but not below it (i.e., v_r is unknown, except on $r = r_b$, where $v_r = 0$). Contrary to the main flow within the core, which is responsible for dynamo action, our flow $\vec{v}$ is generated by a surfacic pressure at the CMB. It is expected to concern a layer with a certain thickness Δ in the upper part of the core and to present upwellings at the maxima of $p(\theta, \phi)$, or of $-\Pi(\theta, \phi)$, and downwellings at its minima.

4.2.2. The Magnetic Anomaly: A Simple Kinematic Model

We address now the computation of the magnetic anomaly generated by a flow in the upper layers of the core which might be induced by the topography of the CMB. We will simply use an existing model, a kinematic 2-D two-scale model [see *Braginsky and Le Mouël*, 1993, Figure 2]. The CMB is the plane $z = 0$, the z axis being oriented downward perpendicular to the horizontal x axis. Below a limit layer of thickness Δ at the top of the outer core, the model contains a large volume ($z \geq \Delta$) in which convective motions in the form of rolls take place. The 2-D velocity field $\vec{v}(x, z)$ is periodic in space with a wavelength $\lambda = 2\pi/k$, and in time with a period $T = 2\pi/\omega$, we take $T = 20$ years (see section 2.2):

$$\vec{v} = \begin{cases} \vec{v}^0(x, z)e^{-i\omega t} & \text{in the volume, } z \geq \Delta, \\ \vec{v}^\Delta(x, z)e^{-i\omega t} & \text{at the top the core, } 0 < z < \Delta, \end{cases} \tag{14}$$

where

$$v_x^0(x, z) = +v_0 e^{-k(z-\Delta)} \sin(kx), \tag{15}$$

$$v_z^0(x, z) = -v_0 e^{-k(z-\Delta)} \cos(kx), \tag{16}$$

$$v_x^\Delta(x, z) = -\frac{v_0}{k\Delta} \sin(kx), \tag{17}$$

$$v_z^\Delta(x, z) = -\frac{v_0 z}{\Delta} \cos(kx). \tag{18}$$

As shown in Figure 10, the flow in the Δ layer is different in nature from the flow underneath but connected to this volume flow and fed by it. However simple, this model contains some of the requirements introduced above: limited vertical extension, vertical component of the flow-simulating upwellings and downwellings, and concentration in the layer of depth Δ. Here following *Braginsky and Le Mouël* [1993] and *Jault and Le Mouël* [1993], we choose, somewhat arbitrarily, $\Delta = 30$ km. v_z is continuous at the interface $z = \Delta$ and cancels at $z = 0$; v_x is much larger in the uppermost layer than in the main body of the core (i.e., $k\Delta \ll 1$) and presents a discontinuity (a shear) at the boundary $z = \Delta$. Then,

$$v_0 = k\,\Delta\,v. \tag{19}$$

v being the estimate given in section 4.2.1 (see equation (13)). Using the v value computed for $\|h_n\| = 0.3$ m ($\|h_n\| = 3$ m), we obtain $v_0 = 1.50 \times 10^{-4}$ m s^{-1} ($v_0 = 1.50 \times 10^{-3}$ m s^{-1}).

For the correspondence between the wave number k in the plane geometry and the harmonic component of degree n in the spherical one, we take $k = 2\pi/\lambda = n/r_b = 1.7 \times 10^{-6}$ m^{-1}. Then, $\lambda = 3.70 \times 10^6$ m for $n = 6$. We then evaluate the secondary field $\vec{b}(b_x, b_z)$ induced by the flow interacting with the main field $\vec{B_0}$ generated by the dynamo action using the linearized induction equation

$$-i\omega\vec{b} - \eta\nabla^2\vec{b} = B_0\partial_z\vec{v}, \tag{20}$$

where η is the core magnetic diffusivity. At our degree of simplification it is enough to take $\vec{B_0} = B_0\vec{z}$. *Braginsky and Le Mouël* [1993] have computed $\vec{b}(x,z)e^{i\omega t}$, and, at the CMB for $r = r_b$ and $z = 0$, they found

$$b_x(x,0) = b_x^{\Delta}(x,0) = +b_0 a(\omega)\sin(kx)e^{-i\omega t}, \tag{21}$$

$$b_z(x,0) = b_z^{\Delta}(x,0) = -b_0 a(\omega)\cos(kx)e^{-i\omega t}. \tag{22}$$

The expressions of b_0 and $a(\omega)$ are given in Appendix A. With the values $k = 1.7 \times 10^{-6}$ m^{-1}, $\eta = 2$ m^2 s^{-1}, $\omega = 10^{-8}$ s^{-1}, $v_0 = 1.50 \times 10^{-4}$ m s^{-1} ($\|h_6\| = 0.3$ m), $T = 2\pi/\omega \approx 20$ years (see section 2), and $B_0 = 3 \times 10^5$ nT, it comes

$$b_0 a(\omega) = Ae^{i\theta} \qquad \text{with} \qquad A = 1.26 \times 10^5 \text{ nT}.$$

An A value equal to 1.26×10^6 nT is obtained for $v_0 = 1.50 \times 10^{-3}$ m s^{-1} (and a corresponding topography of amplitude $\|h_6\| = 3$ m).

Taking the vertical component of the magnetic field at the Earth's surface $z = -D = -2900$ km, we have

$$b_z(x,-D) = -Ae^{i\theta}e^{-kD}\cos(kx)e^{-i\omega t}. \tag{23}$$

Finally, to compare with observations (Figure 1), we can write

$$\frac{\mathrm{d}^2 b_z}{\mathrm{d}t^2} = \omega^2 Ae^{i\theta}e^{-kD}\cos(kx)e^{-i\omega t}.$$

For $T = 20$ years and a topography amplitude $\|h_6\| = 0.3$ m, we find an amplitude for

$$\frac{\mathrm{d}^2 b_z}{\mathrm{d}t^2} \approx 86 \text{ nT yr}^{-2}.$$

A value of 860 nT yr^{-2} is obtained for $\|h_6\| = 3$ m.

Note that we do not suppose as usually the frozen flux approximation (a diffusive term enters equation (20)). The reason is the value of the phase difference observed between the gravity and the magnetic anomalies (see section 2 and Figure 1). Let us now consider the phase difference Θ between the velocity v_0 and the magnetic anomaly b (i.e., the phase of $a(\omega)$ as we take the velocity v_0 in phase with the relief h and the pressure p). With the adopted parameter values, we find $\Theta \approx -120°$ so that the second derivative of the magnetic anomaly lags the velocity by 60° (we use here the time factor $e^{-i\omega t}$). Coming back to the observations and Figure 1,

we admitted that the gravimetric anomaly δg and the second time derivative $d^2\vec{B}/dt^2$ were in phase. In the classical computations of the magnetic anomaly generated by a flow at the top of the core in the frozen flux approximation (infinite conductivity) and, e.g., tangential geostrophy, the phase shift between the flow and the magnetic anomaly is 90°. The present model with finite conductivity ($\eta = 1/(\mu\sigma) = 2$, where σ is the electrical conductivity and μ the magnetic permeability) allows one to act on the phase. The agreement between the model production and the observation is improved (from 90° to 60°). It could be reduced by varying the considered parameters; taking into account the large uncertainties, we content ourselves with this result.

Note that the estimates of b at the CMB may be high, of the same order of magnitude as B_0, the standing field. In this case, the linearized induction equation (equation (20)) may be no longer valid. Our estimates can then be considered as upper limits of b [*Braginsky and Le Mouël*, 1993; *Jault and Le Mouël*, 1991].

5. Discussion and Conclusion

In our crystallization-dissolution model (section 3), the solid-liquid interface between the mantle and the core appears to be fractal, generated by a gradient of concentration of either solid silicate (from the top) or liquid iron (from the bottom) cells. The CMB can be described as a percolation front that emerges spontaneously from our dissolution-crystallization process. This solid-liquid interface has a very small thickness if compared to the horizontal length of the system. Using the predictive scaling law derived from the outputs of the gradient percolation model (Figure 5), it seems reasonable to assume that fluctuations on the order of 10 m may occur at length scales comparable to the characteristic length of the CMB ($\sim 10^4$ km). The proposed mechanism does not suppose an important infiltration of the iron into the mantle. Some other mechanisms described in section 3.1 are probably more efficient to perform this penetration of iron at a larger distance from the CMB [*Kanda and Stevenson*, 2006; *Otsuka and Karato*, 2012]. Nevertheless, these mechanisms are slow, certainly much slower than the infiltration-dissolution process, which is a dynamic process, in continuous renewal. In fact, the main reason of the efficiency of the mechanism to create (coupled) gravity and magnetic anomalies is that it takes full effect of the difference of density between oxides and iron. Exchanges are made in a very thin layer around the CMB so that no long vertical transport of the liquid alloy is needed.

Given the large density contrast between the mantle and the core, an amplitude of a couple meters in topography might generate significant variations of the gravity field at the surface of the Earth. In fact, even heights of the order of tens of centimeters are enough to produce anomalies with an amplitude comparable with that reported in Figure 1 (i.e., 500 nGal). The main issue is whether such a relief with tens of centimeters of amplitude may occur on timescale of decades as required by our observations (section 1). Our numerical simulations show that a transport mechanism much faster than molecular diffusion is required. We can call, as frequently done, for some kind of turbulent diffusivity. Given the complex interactions between the flow and the topography, such an enhancement of transport efficiency may be expected, especially in turbulent boundary layers. On the other hand, coherent flow structures may also concentrate or disperse the dissolved silicate material at the top of the core. As a consequence, they may result in the formation of large erosional or depositional areas where rapid variations of the mass density profile can occur. We have shown that even using only molecular diffusion, rates of deposition of about 10 cm yr^{-1} can be reached. Thus, we propose that the integrated effect of a range of geomorphic processes may be responsible for an evolving topography and measurable changes in gravity at the Earth's surface at a decadal timescale.

This topography exerts a pressure on the fluid core at the CMB, which is accompanied by an additional flow in the upper layers of the core. Interacting with the main field of the dynamo, this flow generates a secondary magnetic field b. With reasonable values of the considered parameters, its second time derivative at the Earth's surface may be of some 60 nT yr^{-2} for $h \approx 20$ cm, 10 times larger for $h \approx 2$ m, comparable with the observed magnetic anomaly (Figure 1).

In the present paper, we have proposed a mechanism capable of generating simultaneous gravimetric and magnetic signals at the Earth's surface, with reasonable amplitude and phase shift between them. The amplitude of the predicted gravimetric and magnetic anomalies are not only in agreement with the observed ones (Figure 1) but also require the same range of topographic variations at the CMB. Figure 11 synthesizes our results and shows that for a harmonic component of degree 6 (i.e., 1800 km at the CMB), both anomalies require an amplitude of approximately 20 cm for the changes in topography. This amplitude of the topography and the corresponding rate of change in elevation ($\approx$ cm yr^{-1}) are of the same order of magnitude as the

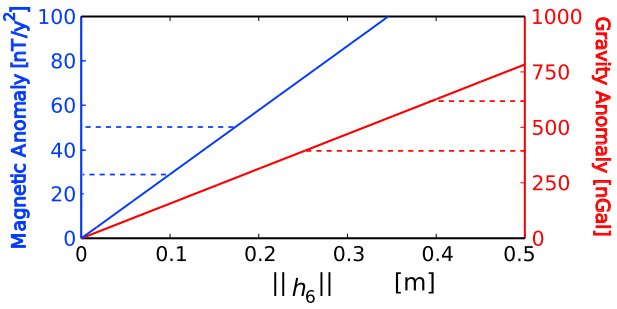

Figure 11. Amplitude of the gravimetric (red) and magnetic anomalies (blue) with respect to the amplitude of the topography of the CMB for a harmonic component of degree 6 (see sections 4.1 and 4.2). The dashed lines show the ranges of the amplitude of both signals observed in Figure 1. We note a fair agreement between the amplitude of the CMB predicted by the gravimetric and the magnetic models, typically a couple of decimeters. This amplitude of the topography and the corresponding rate of change in elevation ($\approx$ cm yr^{-1}) are also on the same order of magnitude as the one predicted by the cellular automaton model (see section 3).

one independently predicted by the cellular automaton model (see section 3). Obviously, many uncertainties remain in the evaluation of the changes in topography and both the magnetic and gravimetric anomalies. However, all estimates together encourage to examine further the effect of geomorphic processes at the CMB.

A difficulty is outstanding: the magnetic signals potentially generated by the dissolution-crystallization process and the regular secular variation of the main field generated by the dynamo in the core may have time constant which are not far away; so their separation may be out of reach in the present state of things. Obviously, long-time observation would be required. Satellites will provide us with these observations in the next few decades.

Appendix A

Following the BLM model proposed by *Braginsky and Le Mouël* [1993], the expression of b_0 and $a(\omega)$ are

$$b_0 = \frac{B_0 v_0}{2\eta k}$$

and

$$a(\omega) = \frac{2k}{k+q}\left(\left(\frac{k}{k+q}+\frac{1}{q\Delta}\right)e^{-q\Delta}-\frac{1}{q\Delta}\right),$$

where

$$q = k\left(1-\frac{i\omega}{\eta k^2}\right)^{1/2}$$

despite its elementary nature, the BLM model needs some tedious computations. A simpler model leading to grossly similar results has been proposed by *Jault and Le Mouël* [1991].

Acknowledgments
We thank Olivier Rozier for his help in developing ReSCAL, the numerical model used to compute the CMB. The Real-Space Cellular Automaton Laboratory (ReSCAL) is a free software under the GNU general public license. The source codes can be downloaded from http://www.ipgp.fr/rescal. We are grateful to Jean-Paul Poirier for helpful discussions about core-mantle boundary processes. We also thank Laurent Métivier and Marianne Greff-Lefftz for useful discussions concerning the gravimetric anomalies due to the mantle deformations. We acknowledge financial support from the UnivEarthS LabEx program of Sorbonne Paris Cité (ANR-10-LABX-0023 and ANR-11-IDEX-0005-02) and the French National Research Agency (ANR-12-BS05-001-03/EXO-DUNES).

References

Ahnert, F. (1987), Approaches to dynamic equilibrium in theoretical simulations of slope development, *Earth Surf. Processes Landforms*, *12*(1), 3–15.
Alterman, Z., H. Jarosch, and C. Pekeris (1959), Oscillations of the Earth, *Proc. R. Soc. London, Ser. A*, *252*(1268), 80–95.
Braginsky, S. (1984), Short-period geomagnetic secular variation, *Geophys. Astrophys. Fluid Dyn.*, *30*(1-2), 1–78.
Braginsky, S., and J.-L. Le Mouël (1993), Two-scale model of a geomagnetic field variation, *Geophys. J. Int.*, *112*, 147–158.
Bruinsma, S., J.-M. Lemoine, R. Biancale, and N. Valès (2010), CNES/GRGS 10-day gravity field models (release 2) and their evaluation, *Adv. Space Res.*, *45*, 587–601.
Buffett, B. A., and C. T. Seagle (2010), Stratification of the top of the core due to chemical interactions with the mantle, *J. Geophys. Res.*, *115*, B04407, doi:10.1029/2009JB006751.
Buffett, B. A., E. J. Garnero, and R. Jeanloz (2000), Sediments at the top of Earth's core, *Science*, *290*(5495), 1338–1342.
Chinnery, M. A. (1975), The static deformation of an Earth with a fluid core: A physical approach, *Geophys. J. Int.*, *42*(2), 461–475.
Christensen, U., and J. Aubert (2006), Scaling properties of convection-driven dynamos in rotating spherical shells and application to planetary magnetic fields, *Geophys. J. Int.*, *166*(1), 97–114.

Dumberry, M. (2010), Gravity variations induced by core flows, *Geophys. J. Int.*, *180*(2), 635–650.
Dumberry, M., and J. Bloxham (2004), Variations in the Earth's gravity field caused by torsional oscillations in the core, *Geophys. J. Int.*, *159*(2), 417–434.
Essam, J. W. (1972), Percolation and cluster size, in *Phase Transitions and Critical Phenomena*, vol. 2, edited by C. Domb and H. S. Green, pp. 197–270, Academic Press, New York.
Garnero, E. J., D. V. Helmberger, and S. P. Grand (1993a), Constraining outermost core velocity with *SmKS* waves, *Geophys. Res. Lett.*, *20*(22), 2463–2466, doi:10.1029/93GL02823.
Gilbert, G. (1877), Report on the geology of the Henry Mountains, in *U.S. Geographical and Geological Survey of the Rocky Mountain Region*, U.S. Gov. Print. Off., Washington, D. C.
Gouyet, J. F., and M. Rosso (2005), Diffusion fronts and gradient percolation: A survey, *Physica A*, *357*, 86–96.
Greff-Lefftz, M., M. Pais, and J.-L. Le Mouël (2004), Surface gravitational field and topography changes induced by the Earth's fluid core motions, *J. Geod.*, *78*(6), 386–392.
Grossman, T., and A. Aharony (1987), Accessible external perimeters of percolation clusters, *J. Phys. A*, *20*, 1193–1201.
Heimsath, A. M., W. E. Dietrich, K. Nishiizumi, and R. C. Finkel (1997), The soil production function and landscape equilibrium, *Nature*, *388*(6640), 358–361.
Helffrich, G., and S. Kaneshima (2010), Outer-core compositional stratification from observed core wave speed profiles, *Nature*, *468*(7325), 807–810.
Hinderer, J., H. Legros, C. Gire, and J. Le Mouël (1987), Geomagnetic secular variation, core motions and implications for the Earth's wobbles, *Phys. Earth Planet. Inter.*, *49*, 121–132.
Hinze, J. (1972), *Turbulence*, McGraw-Hill, New York.
Holschneider, M. (1995), *Wavelets: An Analysis Tool*, Oxford Univ. Press, New York.
Jault, D., and J.-L. Le Mouël (1991), Physical properties at the top of the core and core surface motions, *Phys. Earth Planet. Inter.*, *68*, 76–84.
Jault, D., and J. Le Mouël (1993), Circulation in the liquid core and coupling with the mantle, *Adv. Space Res.*, *13*(11), 221–233.
Kanda, R. V., and D. J. Stevenson (2006), Suction mechanism for iron entrainment into the lower mantle, *Geophys. Res. Lett.*, *33*, L02310, doi:10.1029/2005GL025009.
Le Mouël, J.-L. (1984), Outer-core geostrophic flow and secular variation of Earth's geomagnetic field, *Nature*, *311*, 734–735.
Le Mouël, J.-L., C. Narteau, M. Greff, and M. Holschneider (2005), Dissipation at the core-mantle boundary on a small scale topography, *J. Geophys. Res.*, *111*, B04413, doi:10.1029/2005JB003846.
Lesur, V., I. Wardinski, M. Rother, and M. Mandea (2008), GRIMM—The GFZ Reference Internal Magnetic Model based on vector satellite and observatory data, *Geophys. J. Int.*, *173*, 382–394, doi:10.1111/j.1365-246X.2008.03724.x.
Lesur, V., I. Wardinski, M. Hamoudi, and M. Rother (2010), The second generation of the GFZ Reference Internal Magnetic Model: GRIMM-2, *Earth Planets Space*, *62*, 765–773, doi:10.5047/eps.2010.07.007.
Ligrani, P. M., and R. J. Moffat (1986), Structure of transitionally rough and fully rough turbulent boundary layers, *J. Fluid Mech.*, *162*, 69–98.
Lloyd, D., and D. Gubbins (1990), Toroidal fluid motion at the top of the Earth's core, *Geophys. J. R. Astron. Soc.*, *100*, 455–467.
Mandea, M., R. Holme, A. Pais, K. Pinheiro, A. Jackson, and G. Verbanc (2010), Geomagnetic jerks: Rapid core field variations and core dynamics, *Space Sci. Rev.*, *155*, 147–175, doi:10.1007/s11214-010-9663-x.
Mandea, M., I. Panet, V. Lesur, O. de Viron, M. Diament, and J. Le Mouël (2012), Recent changes of the Earth's core derived from satellite observations of magnetic and gravity fields, *Proc. Natl. Acad. Sci.*, *109*(47), 19,129–19,133.
Narteau, C. (2007), Formation and evolution of a population of strike-slip faults in a multiscale cellular automaton, *Geophys. J. Int.*, *168*, 723–744.
Narteau, C., J.-L. Le Mouël, J. Poirier, E. Sepúlveda, and M. G. Shnirman (2001), On a small scale roughness of the core-mantle boundary, *Phys. Earth Planet. Inter.*, *191*, 49–61.
Olsen, N., M. Mandea, T. Sabaka, and L. Toffner-Clausen (2010), The CHAOS-3 geomagnetic field model and candidates for the 11th generation IGRF, *Earth Planets Space*, *62*(10), 719–727.
Olsen, N., H. Luhr, C. C. Finlay, T. J. Sabaka, I. Michaelis, J. Rauberg, and L. Toffner-Clausen (2014), The CHAOS-4 geomagnetic field model, *Geophys. J. Int.*, *197*(2), 815–827, doi:10.1093/gji/ggu033.
Otsuka, K., and S.-I. Karato (2012), Deep penetration of molten iron into the mantle caused by a morphological instability, *Nature*, *492*(7428), 243–246.
Ozawa, H., K. Hirose, M. Mitome, Y. Bando, N. Sata, and Y. Ohishi (2009), Experimental study of reaction between perovskite and molten iron to 146 GPa and implications for chemically distinct buoyant layer at the top of the core, *Phys. Chem. Miner.*, *36*(6), 355–363.
Pfeifer, P., and M. Obert (1989), Fractals: Basic concepts and terminology, in *The Fractal Approach to Heterogeneous Chemistry*, pp. 11–43, John Wiley, New York.
Poirier, J., V. Malavergne, and J.-L. Le Mouël (1998), Is there a fine conductive layer at the base of the mantle?, in *The Core Mantle Boundary Region, AGU Monogr.*, pp. 131–137, AGU, Washington, D. C.
Poirier, J.-P. (2000), *Introduction to Physics of the Earth's Interior*, Cambridge Univ. Press, Cambridge, U. K.
Poirier, J.-P., and J. L. Le Mouël (1992), Does infiltration of core material into the lower mantle affect the observed geomagnetic field?, *Phys. Earth Planet. Inter.*, *73*, 29–37.
Rozier, O., and C. Narteau (2014), A Real Space Cellular Automaton Laboratory, *Earth Surf. Processes Landforms*, *39*, 98–109, doi:10.1002/esp.3479.
Sapoval, B., A. Baldassarri, and A. Gabrielli (2004), Self-stabilized fractality of sea-coasts through erosion, *Phys. Rev. Lett.*, *93*, 098501.
Sapoval, M., B. Rosso, and J. F. Gouyet (1985), The fractal nature of a diffusion front and relation to percolation, *J. Phys. Lett.*, *46*, 149–156.
Stauffer, D., and A. Aharony (1994), *Introduction to Percolation Theory*, Taylor and Francis, London.
Stevenson, D. J. (2012), Fluctuating gravity of Earth's core, *Proc. Natl. Acad. Sci. U.S.A.*, *109*(47), 19,039–19,040.
Takafuji, N., K. Hirose, M. Mitome, and Y. Bando (2005), Solubilities of O and Si in liquid iron in equilibrium with (Mg, Fe) SiO3 perovskite and the light elements in the core, *Geophys. Res. Lett.*, *32*, L06313, doi:10.1029/2005GL022773.
Tanaka, S. (2007), Possibility of a low P-wave velocity layer in the outermost core from global *SmKS* waveforms, *Earth Planet. Sci. Lett.*, *259*(3), 486–499.
Tapley, B. D., S. Bettadpur, J. C. Ries, P. F. Thompson, and M. M. Watkins (2004), GRACE measurements of mass variability in the Earth system, *Science*, *305*, 503–505.